Check for updates

OPEN

Refractive index gas sensor based on the Tamm state in a one-dimensional photonic crystal: Theoretical optimisation

Zaky A. Zaky, Ashour M. Ahmed✉, Ahmed S. Shalaby & Arafa H. Aly

Gas sensors are important in many fields such as environmental monitoring, agricultural production, public safety, and medical diagnostics. Herein, Tamm plasmon resonance in a photonic bandgap is used to develop an optical gas sensor with high performance. The structure of the proposed sensor comprises a gas cavity sandwiched between a one-dimensional porous silicon photonic crystal and an Ag layer deposited on a prism. The optimised structure of the proposed sensor achieves ultra-high sensitivity ($S = 1.9 \times 10^5$ nm/RIU) and a low detection limit (DL $= 1.4 \times 10^{-7}$ RIU) compared to the existing gas sensor. The brilliant sensing performance and simple design of the proposed structure make our device highly suitable for use as a sensor in a variety of biomedical and industrial applications.

Gas sensing has different applications in many fields such as the food industry, medicine, safety, environment, agriculture, and cosmetic[1,2]. For example, the detection of volatile organic compounds such as acetone and toluene in exhaled breath is used as a biomarker for many diseases[3,4]. In addition, the determination of the concentration of harmful gases such as CO_2 and N_2O can be applied as an environmental pollution monitor[5].

Currently, optical gas sensors are of great interest to researchers because they do not require complicated radioactive/fluorescent labels[6,7]. Surface plasmon resonance, Tamm plasmon (TP) resonance, waveguide, and photonic crystal are all examples of platforms for optical sensing[8–12].

Photonic crystals (PCs) are useful for a wide range of biomedical and environmental sensing applications. This is due to an impressive set of relevant properties, such as ultrahigh sensitivity, low detection limit, and fast response time[13,14]. PC refers to a range of materials characterised by a periodic refractive index along one, two, or three dimensions (1DPC, 2DPC, or 3DPC, respectively). The propagation of electromagnetic waves in PCs can be controlled because of the photonic bandgap (PBG)[15–17]. 1DPCs are more appropriate for most applications, given their low cost and ease of fabrication compared to 2DPCs and 3DPCs[18].

Recently, PCs have been widely used in various sensor systems. A high-precision gas index sensor, which was proposed by Jágerská *et al.*, reached a sensitivity of 510 nm/RIU based on a PC air-slot cavity[19]. Hua-Jun studied a surface plasmon resonance nanocavity antenna array for use as a gas sensor with a high sensitivity of 3200 nm/RIU[20]. Wang *et al.* suggested a guided-mode resonance gas sensor with a sensitivity as high as 748 nm/RIU[21]. Pevec and Donlagic designed a fiber-optic Fabry-Perot gas sensor with a sensitivity of 1550 nm/RIU[22]. García-Rupérez *et al.* presented a highly sensitive device for antibody detection using the slow light regime of a PC waveguide[23]. Chen *et al.* designed a PC/Ag/graphene structure to function as a refractive index sensor based on the Tamm state, with a numerical sensitivity of 1178.6 nm/RIU[24]. Auguié *et al.* studied TP resonance at the interface between a metal/mesoporous PC. The numerical results showed that the sensitivity was approximately 55 nm/RIU[25].

Recently, 1DPCs based on multilayers of porous silicon (PSi) have become an effective solution for the design of novel biosensors[26–28]. PSi characteristically provides high surface area and low mass within small volumes. The optical properties of PSi can be controlled by changing the size of the pores and/or material that fills the pores[27]. Moreover, PSi is compatible with integrated electronic circuits.

In contrast, TP resonance is used as an optical sensor technology with high performance. TPs can be created inside the bandgap by adding a metal layer in front of the 1DPC[25]. The wavelength location of the TP resonant dip

TH-PPM Group, Physics Department, Faculty of Sciences, Beni-Suef University, Beni-Suef, Egypt. ✉e-mail: ashour.mohamed@science.bsu.edu.eg
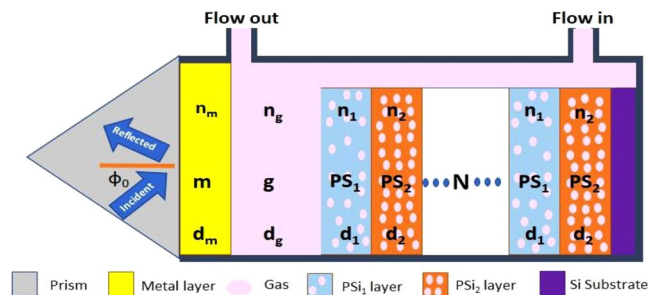
Figure 1. Schematic of the proposed biosensor consisting of prism/Ag/gas/(PSi$_1$/PSi$_2$)^N/Si.

can be shifted by changing the effective refractive index of the 1DPC structure or surrounding medium. This is the principle used in the proposed structure for detecting small changes in the refractive index of the gas.

The present work aims to introduce a high-performance gas sensor based on an effective combination of the TP features and novel properties of PSi photonic crystals.

Sensor Design

The proposed sensor consists of a one-dimensional porous silicon photonic crystal (PSi-1DPC) covered with an Ag layer. In addition, there is a cavity layer between the two materials for the gas to be detected. The Ag layer is deposited on a prism of glass ($n_0 = 1.5$)[29–31].

Figure 1 shows a schematic representation of the proposed structure, which is considered as prism/Ag/gas/(PSi$_1$/PSi$_2$)^N/Si, where gas, PSi$_1$, and PSi$_2$ refer to the gas cavity and the first and second PSi layers, respectively. N indicates the period number. The silicon layer acts as a substrate for the sensor.

The gas sample is injected into the inlet, which is in contact with the upper surface of the structure. This allows the gas to fill the cavity layer and pores of PSi, as shown in Fig. 1.

The refractive index of Ag was obtained from the Drude model[32–34]:

$$n_m = \sqrt{1 - \omega_p^2/(\omega^2 + i\,\gamma\,\omega)}, \tag{1}$$

where the plasma frequency and damping factor are represented by $\omega_p = 2.18$ PHz and $\gamma = 4.353$ THz, respectively[35]. Ag was selected because it has a relatively low imaginary part of the dielectric constant (low absorption loss) compared to gold, platinum, and copper[36].

The refractive index of silicon (n_{Si}) is given by[37]:

$$n_{Si} = \sqrt{\left(1 + \frac{10.6684293\,\lambda^2}{\lambda^2 - 0.301516485^2} + \frac{0.0030434748\,\lambda^2}{\lambda^2 - 1.13475115^2} + \frac{1.54133408\,\lambda^2}{\lambda^2 - 1104^2}\right)}, \tag{2}$$

where λ is the wavelength (μm). The porosities of the PSi$_1$ and PSi$_2$ layers are 32% and 74%, respectively, based on the results of a previous experimental work[38].

Multilayer PSi-1DPC can be prepared by electrochemical etching of a silicon wafer using hydrogen fluoride as the electrolyte[28,38–41].

Theoretical Model

The transfer matrix method (TMM) is used to study the interaction between the incident electromagnetic (EM) waves (S-polarized) and the proposed structure. The details of TMM can be found in many articles[42–46]. The following matrices describe the proposed structure:

$$H = \left(h_m\right)\left(h_{gas}\right)(h_1 h_2)^N = \begin{pmatrix} H_{11} & H_{12} \\ H_{21} & H_{22} \end{pmatrix} \tag{3}$$

where h_1, h_2, h_{gas} and h_m are the characteristic matrix for PSi$_1$, PSi$_2$, the gas sample, and the metallic layer. H_{11}, H_{12}, H_{21}, and H_{22} are the transfer matrix elements for the total structure. The following equation gives the reflection coefficient:

$$r = \frac{(H_{11} + H_{12}\,p_s)p_0 - (H_{21} + H_{22}\,p_s)}{(H_{11} + H_{12}\,p_s)p_0 + (H_{21} + H_{22}\,p_s)} \tag{4}$$
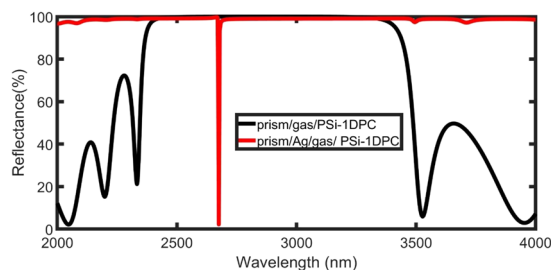
Where $p_0 = n_0 \cos\varphi_0$ (for prism) and $p_s = n_s \cos\varphi_s$ (for Si substrate). Also, φ_0 indicates the incident angle of the electromagnetic waves from the prism to the structure.

Finally, the reflectance of the proposed structure is given by:

$$R(\%) = 100x|r^2| \tag{5}$$
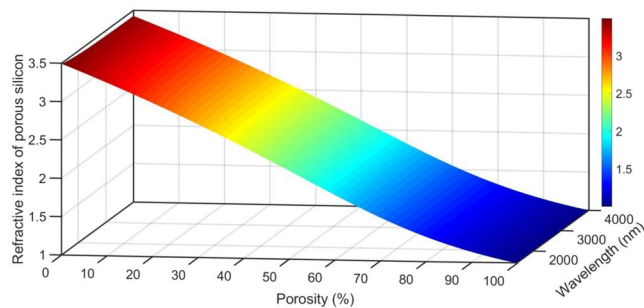
Figure 2. Changes in the n_{Psi} layer as a function of wavelength and porosity.

Figure 3. Reflectance for prism/gas/ PSi-1DPC and prism/ Ag/gas/ PSi-1DPC as a function of the wavelength with a normal incident angle, N = 8, $d_{gas} = 4000$ nm, $n_{gas} = 1.00026$, and $d_m = 30$ nm.

Results and Discussions

In this section, we calculate the refractive index of the PSi (n_{Psi}). Next, we study how the performance of our sensor is affected by changes in the gas refractive index, number of periods, metallic layer thickness, refractive index of the prism, layer thickness of the gas, and angle of incidence of the electromagnetic waves.

Refractive index of porous silicon n_{Psi}. The index of refraction of the PSi layer (n_{Psi}) filled with gas can be obtained by applying Bruggeman's effective medium approximation[26,47,48]:

$$n_{Psi} = 0.5\sqrt{\mathcal{M} + \sqrt{\mathcal{M}^2 + 8n_{si}^2 n_{gas}^2}}$$
$$\mathcal{M} = 3P\left(n_{gas}^2 - n_{si}^2\right) + \left(2\,n_{si}^2 - n_{gas}^2\right), \tag{6}$$

where n_{Psi}, n_{si}, and n_{gas} are the refractive indices of the PSi layer, silicon, and gas inside the pores, respectively. The refractive index of the PSi layer decreases from 3.50 to 1.00026 as the ratio of the porosity of silicon filled with a gas of refractive index 1.00026 changes from 0% to 100% (Fig. 2).

Reflectance spectra for prism/PSi-1DPC and prism/Ag/gas/PSi-1DPC. In all calculations of the reflectance spectra of the electromagnetic waves, the PSi_1 and PSi_2 layers have thicknesses of $d_1 = 200$ nm and $d_2 = 600$ nm with porosities of 32% and 74%, respectively.

Figure 3 shows the reflectance of the prism/$(PSi_1/PSi_2)^8$/Si as a function of the wavelength (black curve). The gas inside the pore has a refractive index of $n_{gas} = 1.00026$. The number of periods is eight (N = 8) and light is normally incident on the structure ($\varphi_0 = 0°$). As illustrated by this figure, there is a wide PBG (high reflection) owing to the high refractive index contrast between the two layers, PSi_1 and PSi_2. This PBG results from the constructive interference of the reflected waves at the interface between different layers. Outside the PBG, ripples appear in the reflectance spectrum with high reflectance.

For the prism/ Ag/gas/$(PSi_1/PSi_2)^8$/Si structure, the layer of the gas cavity and Ag have thicknesses of $d_{gas} = 4000$ nm and $d_m = 30$ nm, respectively. In this case, the PBG expands, and the ripples outside the bandgap almost disappear (red curve in Fig. 3). In addition, a Tamm resonant dip appears with $\lambda_T = 2675$ nm inside the PBG as a result of the electromagnetic waves confined between the Ag layer and distributed Bragg reflector[26,49,50].

Effect of small changes in the gas refractive index. Figure 4 shows the dip position of the TP resonance for the prism/Ag/gas/$(PSi_1/PSi_2)^8$/Si structure at different gas refractive indices. All parameters were maintained as in the previous case ($d_1 = 200$ nm, $d_2 = 600$ nm, $d_{gas} = 4000$ nm, $d_m = 30$ nm, N = 8, and $\varphi_0 = 0°$). The refractive index of the gas sample (n_{gas}) changes from 1.00026 to 1.00046 ($\Delta n_{gas} = 2 \times 10^{-4}$).

Increasing the refractive index of the gas inside the pores causes an increase in the effective refractive index of the PSi layers. Consequently, the effective refractive index of the prism/ Ag/gas/PSi-1DPC structure increases. This leads to a TP resonance shift to longer wavelengths (red-shift)[34,51], in accordance with Bragg's law.
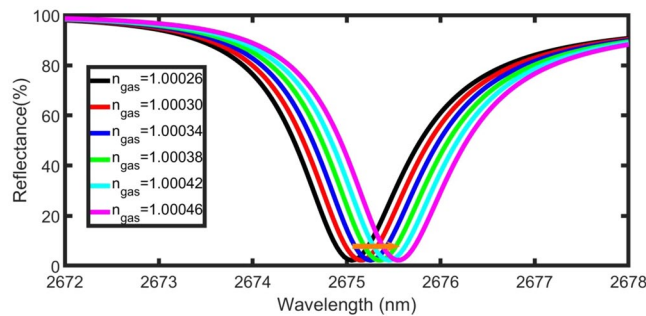
Figure 4. Reflectance spectra of the proposed sensor as a function of wavelength and gas refractive index at $d_{gas} = 4000$ nm, $d_m = 30$ nm, N = 8, and $\varphi_0 = 0°$.
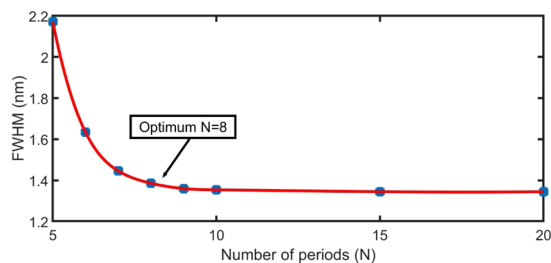
Figure 5. Variation in the FWHM as a function of the number of unit cells N at $d_m = 30$ nm, $n_{gas} = 1.00026$, $n_{prism} = 1.5$, $\varphi_0 = 0°$, and $d_{gas} = 4000$ nm.

The sensitivity (S) is the most important parameter used to characterise the performance of a sensor. It is calculated through the following equation:

$$S = \frac{\Delta\lambda_T}{\Delta n} = \frac{\lambda_T^{1.00046} - \lambda_T^{1.00026}}{1.00046 - 1.00026} = \frac{\lambda_T^{1.00046} - \lambda_T^{1.00026}}{0.0002}, \tag{7}$$

where λ_T is the position of the Tamm resonance dip. By increasing the gas refractive index from 1.00026 to 1.00046, the TP resonance dip is shifted from $\lambda_T = 2675.16$ to 2675.68 nm, as seen in Fig. 4. The sensitivity in these conditions is approximately 2600 nm/RIU.

To achieve the highest performance, different parameters of the proposed sensor, such as the number of periods, metallic layer thickness, prism refractive index, gas layer thickness, and incident angle were optimised.

Effect of number of periods. By increasing the number of periods, the sensitivity does not change (S = 2600 nm/RIU). In addition to the sensitivity, the study of the full width at half maximum (FWHM) of the resonance dip is another significant parameter for the performance of the sensor. A high-performance sensor should have a narrow resonant dip to achieve high resolution[52]. Figure 5 shows the behaviour of the FWHM as a function of the number of unit cells (N), at Ag layer thickness $d_m = 30$ nm, gas layer thickness $d_{gas} = 4000$ nm, $n_{gas} = 1.00026$, $n_{prism} = 1.5$, and normal incidence of electromagnetic waves.

The FWHM value decreases (from 2.17 to 1.39 nm) with an increase in the number of periods from N = 5 to 8. Above N = 8, the FWHM value seems to be constant[25]. Therefore, N = 8 is considered as the optimum number of layers for the next calculation.

Effect of Ag layer thickness. Figure 6 shows the variation in the reflectance of the Tamm resonant dip (R_T) as a function of the Ag layer thickness at $n_{gas} = 1.00026$, $\varphi_0 = 0°$, $d_{gas} = 4000$ nm, $n_{prism} = 1.5$, and N = 8.

When the Ag layer has a thickness of 25 nm, the reflectance of the resonant dip decreases to zero, and the optical energy is consumed by absorption[25]. Hence, strong confined electromagnetic waves occur between the Ag and gas/$(PSi_1/PSi_2)^8$/Si structure[26,49,50], which is crucial for sensing applications. Therefore, $d_m = 25$ nm is considered as the optimum thickness for the Ag layer, because it achieves zero reflectance. When the thickness of the Ag layer differs from the optimal value, the reflectance of the resonant dip increases resulting in the low coupling of the TP, as seen in Fig. 6. This behaviour is similar to the results observed in a previous study[53].

Effect of prism refractive index. To study the effect of the refractive index of the prism on the reflectance of the structure, we changed the refractive index of the prism from 1.4 to 2.5[54,55]. According to the principle of total internal reflection, the critical angle (φ_c) depends on the values of the refractive index of the prism and gas for the prism/ gas/PSi-1DPC structure. The critical angle can be calculated using the following equation:
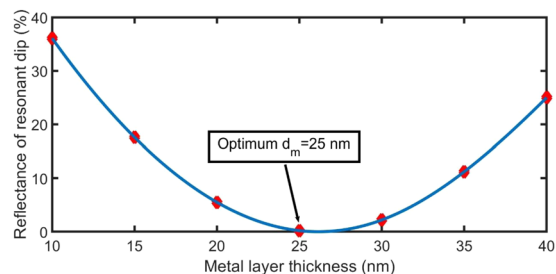
Figure 6. Variation of the reflectance of the resonant dip as a function of the metallic layer thickness at $n_{gas} = 1.00026$, $\varphi_0 = 0°$, $d_{gas} = 4000\,nm$, $n_{prism} = 1.5$, and N = 8.
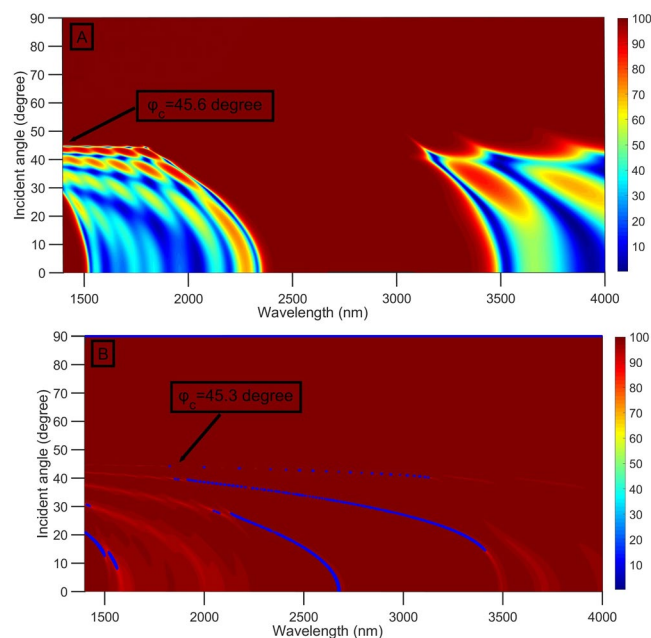
Figure 7. Reflectance spectra as a function of wavelength and incident angle at $n_{gas} = 1.00026$, $d_{gas} = 4000\,nm$, $d_m = 25\,nm$, $n_{prism} = 1.4$ and N = 8 for (**A**) prism/gas/ PSi-1DPC and (**B**) prism/Ag/gas/ PSi-1DPC.

$$\varphi_c = \sin^{-1}\left(\frac{n_{gas}}{n_{prism}}\right)$$

(8)

By taking $n_{gas} = 1.00026$, $d_m = 0$, and $n_{prism} = 1.4$, the value of φ_c equals 45.6°, as clearly shown in Fig. 7A. When n_{prism} increases from 1.4 to 2.5°, the critical angle decreases from 45.6 to 23.6°. Above the critical angle, a total reflection occurs without the appearance of any resonant dips for the prism/gas/ PSi-1DPC (Fig. 7A) and prism/Ag/gas/ PSi-1DPC (Fig. 7B) structures at $n_{prism} = 1.4$. The optimum value of n_{prism} is 1.4, which achieves a high critical angle, and hence a wide range of angles will be studied in the next section.

Effect of gas layer thickness.   An increasing gas layer thickness leads to an increase in the volume fraction (ϕ) of the gas layer and geometric path of the electromagnetic wave inside the 1DPC. Therefore, the interaction between the electromagnetic and gas molecules is enhanced. Hence, the proposed structure will be more sensitive to the changes in the refractive index of the gas by increasing the thickness of the gas layer.

As the gas layer thickness increases from 4000 nm to 10000 nm, the sensitivity increases rapidly from 2600 nm/RIU to 3100 nm/RIU. The sensitivity is not affected when the gas layer thickness is increased to more than 10000 nm, as seen in Fig. 8. This result agrees with previous theoretical and experimental studies[14,56]. A thickness of 10000 nm will be considered as the optimum thickness of the gas layer and used for the subsequent simulations.

Effect of incident angle.   The increase in the incident angle of the S-polarised electromagnetic wave causes a blue-shift (short wavelength) to the Tamm resonance dip, according to the Bragg–Snell law:
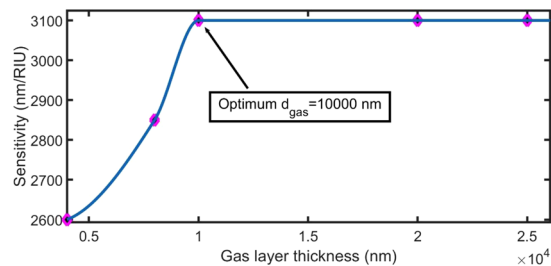
Figure 8. Effect of the gas layer thickness on sensitivity at $N = 8$, $d_m = 25\,nm$, $n_{prism} = 1.4$, and $\varphi_0 = 0°$.
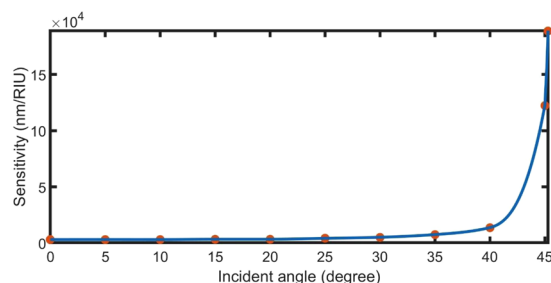
Figure 9. Effect of the incident angle on sensitivity at $N = 8$, $d_3 = 10000\,nm$, $n_{prism} = 1.4$, and $d_m = 25\,nm$.
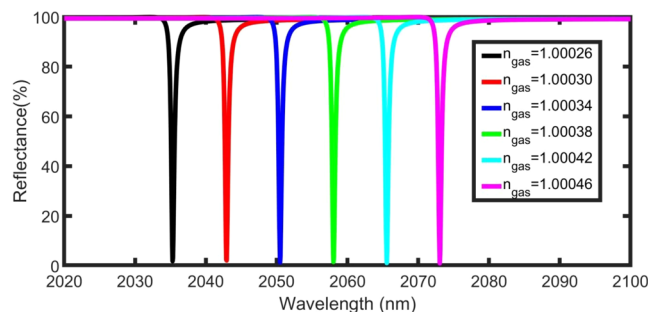
Figure 10. Reflectance spectra of the proposed sensor under optimum conditions with different gas refractive indices.

$$k\,\lambda = 2\,D\sqrt{n_{eff}^2 - \sin^2\varphi_0}\,, \tag{9}$$

where k is the order of diffraction, λ is the wavelength, D is the interplanar spacing, n_{eff} is the effective refractive index, and φ_0 is the angle of incidence.

When the angle of incidence of the electromagnetic waves increases, the wave travels a long geometric path through the gas layer[57]. Therefore, the interactions between the electromagnetic waves and gas molecules are improved. Hence, the sensitivity of the proposed structure is enhanced by increasing the incident angle. By increasing the incident angle from 0 to 45.30º (below φ_c), the sensitivity value increased from 3100 to 188750 nm/ RIU, as shown in Fig. 9. The increase in sensitivity at angles higher than 40° in Fig. 9 is due to the jump in the geometric path of the wave with the increase of the incident angle.

Sensor analysis under optimum conditions. From the above results, the optimum conditions are $N = 8$, $d_m = 25\,nm$, $d_{gas} = 10000\,nm$, $n_{prism} = 1.4$, and $\varphi_0 = 45.3°$. Figure 10 shows the reflectance spectra of the proposed sensor with different gas refractive indices under these optimum conditions. Increasing the gas refractive index leads to shifting the position of the TP mode towards longer wavelengths.

Figure 11 presents a linear fitting of the refractive index of the gas and its dip positions. The slope of the linear fitting refers to the average sensitivity (1.9×10^5 nm/RIU) of our sensor according to the following equation:

$$\lambda_T = 190000\,n_{gas} - 187000, \quad \left(R^2 = 0.999\right) \tag{10}$$
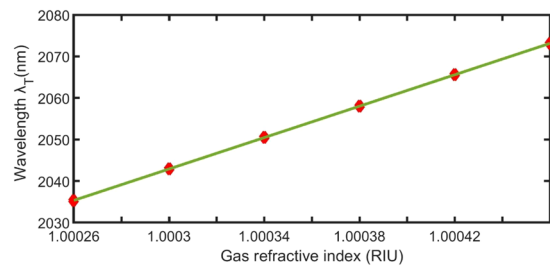
Figure 11. Linear relation between the refractive index of the gas and TP dip positions.

n (RIU)	λ_T (nm)	S (nm/RIU)	FWHM (nm)	FoM $\times 10^5$ (/RIU)	QF $\times 10^3$
1.00026	2035.3	------	0.52	------	4
1.00030	2042.9	190 000	0.52	3.6	4
1.00034	2050.5	190 000	0.52	3.6	4
1.00038	2058.0	187 500	0.52	3.6	4
1.00042	2065.6	190 000	0.52	3.6	4
1.00046	2073.1	187 500	0.52	3.6	4

Table 1. Different parameters of the proposed sensor at optimum conditions.

Year	S (nm / RIU)	FoM (/RIU)	DL (RIU)
2015[61]	970	12.76×10^{-3}	–
2016[62]	450	~800	~1.6×10^{-4}
2016[24]	1179	2.2×10^3	~2.2×10^{-5}
2017[59]	850	–	–
2019[60]	<70	1.04	–
2020[63]	9615	–	–
This work	**1.9×10^5**	**3.6×10^5**	**1.4×10^{-7}**

Table 2. Comparison of sensitivity, figure of merit, and detection limit values of the present work with some experimental and theoretical previous works.

The quality factor (QF), figure of merit (FoM), and detection limit (DL) are usually used to characterise the efficiency and performance of the sensor. An excellent sensor has high QF values that demonstrate the ability of the sensor to have a narrow bandwidth[52]. The QF can be calculated according to the following equation:

$$QF = \frac{\lambda_T}{FWHM} \tag{11}$$

The ratio between the S and the FWHM is referred to as FoM, which is obtained by

$$FoM = \frac{S}{FWHM} \tag{12}$$

The DL is inversely proportional to S and QF according to[58]:

$$DL = \frac{\lambda_T}{20\,S\,QF} \tag{13}$$

Table 1 illustrates that the FoM of our sensor is 3.6×10^5 RIU and the QF is 4×10^3. The high value of the FoM indicates that the proposed sensor has high sensitivity and narrow FWHM simultaneously. In addition, the DL of the sensor is approximately 1.4×10^{-7} RIU, which indicates the smallest detectable refractive index change.

Table 2 compares the values of S, FoM, and DL for the present study with a number of previous experimental and theoretical works[24,59–63] and highlights how the sensitivity of the proposed sensor is higher. Thus, the proposed device with much better performance than hitherto experimentally demonstrated can be constructed[59,60].

Conclusion

We presented a model for a possible large sensitivity gas sensor based on the Tamm state in a one-dimensional photonic crystal. The number of layers, metallic cap layer thickness, prism refractive index, gas layer thickness, and incident angle of the electromagnetic wave were optimised to achieve a biosensor with high performance. The proposed sensor has $S = 1.9 \times 10^5$ nm/RIU, FoM $= 3.6 \times 10^5$ RIU, QF $= 4 \times 10^3$, and DL $= 1.4 \times 10^{-7}$ RIU. The results obtained in the present work motivated us to plan future work focused on the design of photonic crystals as gas sensors for biomedical applications, in particular for the analysis of different gases in the human breath.

References

1. Kanazawa, E. *et al.* Metal oxide semiconductor N2O sensor for medical use. *Sensors and Actuators B: Chemical* **77**, 72–77 (2001).
2. Zhang, Q., Wang, P., Li, J. & Gao, X. Diagnosis of diabetes by image detection of breath using gas-sensitive laps. *Biosensors and Bioelectronics* **15**, 249–256 (2000).
3. Anderson, J. C. Measuring breath acetone for monitoring fat loss. *Obesity* **23**, 2327–2334 (2015).
4. Turner, C., Walton, C., Hoashi, S. & Evans, M. Breath acetone concentration decreases with blood glucose concentration in type I diabetes mellitus patients during hypoglycaemic clamps. *Journal of Breath Research* **3**, 046004 (2009).
5. Islam, M. I. *et al.* Design of single mode spiral photonic crystal fiber for gas sensing applications. Sensing and Bio-Sensing. *Research* **13**, 55–62 (2017).
6. Saarinen, J. J., Weiss, S. M., Fauchet, P. M. & Sipe, J. Optical sensor based on resonant porous silicon structures. *Optics Express* **13**, 3754–3764 (2005).
7. Liedberg, B., Lundström, I. & Stenberg, E. Principles of biosensing with an extended coupling matrix and surface plasmon resonance. *Sensors and Actuators B: Chemical* **11**, 63–72 (1993).
8. Sancho-Fornes, G. *et al.* Disk-based one-dimensional photonic crystal slabs for label-free immunosensing. *Biosensors and Bioelectronics* **126**, 315–323 (2019).
9. Gryga, M., Ciprian, D. & Hlubina, P. in Optical Sensors 2019. 110281P (International Society for Optics and Photonics).
10. Yablonovitch, E. Inhibited spontaneous emission in solid-state physics and electronics. *Physical Review Letters* **58**, 2059 (1987).
11. Shaban, M., Ahmed, A. M., Abdel-Rahman, E. & Hamdy, H. Tunability and sensing properties of plasmonic/1D photonic crystal. *Scientific Reports* **7**, 41983 (2017).
12. Shaban, S. M., Mehaney, A. & Aly, A. H. Determination of 1-propanol, ethanol, and methanol concentrations in water based on a one-dimensional phoxonic crystal sensor. *Applied Optics* **59**, 3878–3885 (2020).
13. Benz, A. *et al.* Terahertz active photonic crystals for condensed gas sensing. *Sensors* **11**, 6003–6014 (2011).
14. Aly, A. H. & Zaky, Z. A. Ultra-sensitive photonic crystal cancer cells sensor with a high-quality factor. *Cryogenics* **104**, 102991 (2019).
15. Aly, A. H. & Elsayed, H. A. Transmittance properties of the one-dimensional metallic-dielectric photonic crystals in near-zero permittivity. Physica Scripta 94 (2019).
16. Aly, A. H., Ahmed, A. M. & Shaban, M. Multilayer angular optical filter as a smart window. Indian Journal of Physics, 1–9 (2019).
17. Aly, A. H., Ameen, A. A., Elsayed, H. A., Mohamed, S. & Singh, M. R. One-dimensional Metallo-superconductor photonic crystals as a smart window. Journal of Superconductivity and Novel Magnetism, 1–6 (2019).
18. Shen, H., Wang, Z., Wu, Y. & Yang, B. One-dimensional photonic crystals: fabrication, responsiveness and emerging applications in 3D construction. *RSC Advances* **6**, 4505–4520 (2016).
19. Jágerská, J., Zhang, H., Diao, Z., Le Thomas, N. & Houdré, R. Refractive index sensing with an air-slot photonic crystal nanocavity. *Optics Letters* **35**, 2523–2525 (2010).
20. Hua-Jun, Z. High sensitivity refractive index gas sensing enhanced by surface plasmon resonance with nano-cavity antenna array. *Chinese Physics B* **21**, 087104 (2012).
21. Wang, L. *et al.* High-sensitive transmission type of gas sensor based on guided-mode resonance in coupled gratings. *Journal of Modern Optics* **65**, 1601–1608 (2018).
22. Pevec, S. & Donlagic, D. Miniature fiber-optic Fabry-Perot refractive index sensor for gas sensing with a resolution of 5x10− 9 RIU. *Optics Express* **26**, 23868–23882 (2018).
23. García-Rupérez, J. *et al.* Label-free antibody detection using band edge fringes in SOI planar photonic crystal waveguides in the slow-light regime. *Optics Express* **18**, 24276–24286 (2010).
24. Chen, Y., Dong, J., Liu, T., Zhu, Q. & Chen, W. Refractive index sensing performance analysis of photonic crystal containing graphene based on optical Tamm state. *Modern Physics Letters B* **30**, 1650030 (2016).
25. Auguié, B., Bruchhausen, A. & Fainstein, A. Critical coupling to Tamm plasmons. *Journal of Optics* **17**, 035003 (2015).
26. Ahmed, A. M. & Mehaney, A. Ultra-high sensitive 1D porous silicon photonic crystal sensor based on the coupling of Tamm/Fano resonances in the mid-infrared region. *Scientific Reports* **9**, 6973 (2019).
27. Pacholski, C. Photonic crystal sensors based on porous silicon. *Sensors* **13**, 4694–4713 (2013).
28. Wang, Z. *et al.* 1D partially oxidized porous silicon photonic crystal reflector for mid-infrared application. *Journal of Physics D: Applied Physics* **40**, 4482 (2007).
29. Xi, J.-Q. *et al.* Omnidirectional reflector using nanoporous SiO2 as a low-refractive-index material. *Optics letters* **30**, 1518–1520 (2005).
30. Hu, D. J. J. & Ho, H. P. Recent advances in plasmonic photonic crystal fibers: design, fabrication and applications. *Advances in Optics and Photonics* **9**, 257–314 (2017).
31. Ahmed, A. M. & Shaban, M. Highly sensitive Au–Fe2O3–Au and Fe2O3–Au–Fe2O3 biosensors utilizing strong surface plasmon resonance. *Applied Physics B* **126**, 1–10 (2020).
32. Aly, A. H. Metallic and superconducting photonic crystal. *Journal of Superconductivity and Novel Magnetism* **21**, 421 (2008).
33. Yu, J. *et al.* Absorption in one-dimensional metallic–dielectric photonic crystals. *Journal of Physics: Condensed Matter* **16**, L51 (2004).
34. Aly, A. H., Ismaeel, M. & Abdel-Rahman, E. Comparative study of the one-dimensional dielectric and metallic photonic crystals. Optics and Photonics. *Journal* **2**, 105 (2012).
35. Ordal, M. A., Bell, R. J., Alexander, R. W., Long, L. L. & Querry, M. R. Optical properties of fourteen metals in the infrared and far-infrared: Al, Co, Cu, Au, Fe, Pb, Mo, Ni, Pd, Pt, Ag, Ti, V, and W. *Applied Optics* **24**, 4493–4499 (1985).
36. Basyooni, M. A., Ahmed, A. M. & Shaban, M. Plasmonic hybridization between two metallic nanorods. *Optik* **172**, 1069–1078 (2018).
37. Salzberg, C. D. & Villa, J. J. Infrared refractive indexes of silicon germanium and modified selenium glass. *JOSA* **47**, 244–246 (1957).
38. Rasson, J., Poncelet, O., Mouchet, S. R., Deparis, O. & Francis, L. A. Vapor sensing using a bio-inspired porous silicon photonic crystal. *Mater. Today Proc* **4**, 5006–5012 (2017).
39. Pavesi, L. Porous silicon dielectric multilayers and microcavities. La Rivista del Nuovo Cimento (1978-1999) 20, 1 (1997).

40. Harraz, F. A. Porous silicon chemical sensors and biosensors: A review. *Sensors and Actuators B: Chemical* **202**, 897–912 (2014).
41. Dang, Z. *et al*. Silicon and porous silicon mid-infrared photonic crystals. *Applied Physics A* **112**, 517–523 (2013).
42. Iwasaka, M. & Asada, H. Floating photonic crystals utilizing magnetically aligned biogenic guanine platelets. *Scientific Reports* **8**, 16940 (2018).
43. Aly, A. H. & Elsayed, H. A. Defect mode properties in a one-dimensional photonic crystal. *Physica B: Condensed Matter* **407**, 120–125 (2012).
44. Lakowicz, J. R. & Badugu, R. (Google Patents, 2018).
45. Aly, A. H. The transmittance of two types of one-dimensional periodic structures. *Materials Chemistry and Physics* **115**, 391–394 (2009).
46. Aly, A. H., Ryu, S.-W. & Wu, C.-J. Electromagnetic wave propagation characteristics in a one-dimensional metallic photonic crystal. *Journal of Nonlinear Optical Physics & Materials* **17**, 255–264 (2008).
47. Patel, P., Mishra, V. & Panchal, A. Theoretical and experimental study of nanoporous silicon photonic microcavity optical sensor devices. Advances in Natural. *Sciences: Nanoscience and Nanotechnology* **3**, 035016 (2012).
48. Salem, M., Sailor, M., Harraz, F., Sakka, T. & Ogata, Y. Electrochemical stabilization of porous silicon multilayers for sensing various chemical compounds. *Journal of Applied Physics* **100**, 083520 (2006).
49. Kumar, S., Shukla, M. K., Maji, P. S. & Das, R. Self-referenced refractive index sensing with hybrid-Tamm-plasmon-polariton modes in sub-wavelength analyte layers. *Journal of Physics D: Applied Physics* **50**, 375106 (2017).
50. Gaspar-Armenta, J. A. & Villa, F. Photonic surface-wave excitation: photonic crystal–metal interface. *JOSA B* **20**, 2349–2354 (2003).
51. Schroden, R. C., Al-Daous, M., Blanford, C. F. & Stein, A. Optical properties of inverse opal photonic crystals. *Chemistry of Materials* **14**, 3305–3315 (2002).
52. Gupta, V. et al. in 2008 International Conference on Information Technology and Applications in Biomedicine. 120-123 (IEEE).
53. Yuan, X. *et al*. Sensitivity–stability-optimized surface plasmon resonance sensing with double metal layers. *Journal of Optics A: Pure and Applied Optics* **8**, 959 (2006).
54. Wu, L. *et al*. Sensitivity improved SPR biosensor based on the MoS2/graphene–aluminum hybrid structure. *Journal of Lightwave Technology* **35**, 82–87 (2016).
55. Lide, D. R. CRC handbook of chemistry and physics. Vol. 85 (CRC press, 2004).
56. Liu, Y. *et al*. Optofluidic vapor sensing with free-space coupled 2D photonic crystal slabs. *Scientific Reports* **9**, 4209 (2019).
57. Aly, A. H., Zaky, Z. A., Shalaby, A. S., Ahmed, A. M. & Vigneswaran, D. Theoretical study of hybrid multifunctional one-dimensional photonic crystal as a flexible blood sugar sensor. Physica Scripta 95 (2019).
58. El Beheiry, M., Liu, V., Fan, S. & Levi, O. Sensitivity enhancement in photonic crystal slab biosensors. *Optics Express* **18**, 22702–22714 (2010).
59. Huang, X. *et al*. An in-line Mach-Zehnder interferometer using thin-core fiber for ammonia gas sensing with high sensitivity. *Scientific reports* **7**, 44994 (2017).
60. Sansierra, M. C., Morrone, J., Cornacchiulo, F., Fuertes, M. C. & Angelomé, P. C. Detection of Organic Vapors Using Tamm Mode Based Devices Built from Mesoporous Oxide Thin Films. *ChemNanoMat* **5**, 1289–1295 (2019).
61. Das, R., Srivastava, T. & Jha, R. On the performance of Tamm-plasmon and surface-plasmon hybrid-mode refractive-index sensor in metallo-dielectric heterostructure configuration. *Sensors and Actuators B: Chemical* **206**, 443–448 (2015).
62. Qian, X. & Zhao, Y. Zhang, Y.-n. & Wang, Q. Theoretical research of gas sensing method based on photonic crystal cavity and fiber loop ring-down technique. *Sensors and Actuators B: Chemical* **228**, 665–672 (2016).
63. Sharma, S., Chaudhary, V. S. & Kumar, D. Design of chemical sensor based on dual core photonic crystal fiber. Materials Today: Proceedings (2020).

Author contributions

Z.A. Zaky performed numerical simulations and wrote the main manuscript text. A.M. Ahmed invented the original idea for the study, discussed the data, and contributed to the writing of the main manuscript. A.S. Shalaby discussed the results, contributed in writing and revising the manuscript. A.H. Aly analyzed the data, discussed the results and supervised this work.

Competing interests

The authors declare no competing interests.

Additional information

Correspondence and requests for materials should be addressed to A.M.A.

Reprints and permissions information is available at www.nature.com/reprints.

Publisher's note Springer Nature remains neutral with regard to jurisdictional claims in published maps and institutional affiliations.